GLOBAL MODELS OF THE SOLAR WIND INTERACTION WITH VENUS

J. G. LUHMANN
University of California at Berkeley

S. H. BRECHT
Berkeley Research Associates

J. R. SPREITER
Stanford University

S. S. STAHARA
RMA Associates

R. S. STEINOLFSON
Southwest Research Institute

and

A. F. NAGY
University of Michigan

In-depth observational analyses of the Venus-solar wind interaction over the last decade have both stimulated and responded to the synergistic development of global theoretical models. The latest global models include mass-loaded gas dynamic magnetosheath models, MHD models of the solar wind interaction with conducting spheres representing the planetary ionosphere, hybrid models in which both solar wind and planetary ion kinetics are included, and test particle models wherein ions are introduced into prescribed global field models. Each gives somewhat different but complementary insights into the physical consequences of the solar wind interaction with a planetary atmosphere. In particular, the gas dynamic magnetosheath and MHD models allow us to interpret the interplanetary magnetic field and solar wind flow disturbances created by the Venus obstacle. They also give us background fields to be used in test particle investigations of the characteristics of the planetary pick-up ion population. The global hybrid simulations uniquely combine self-consistent aspects of both, although they are constrained to lower spatial resolutions by current computational constraints. Several of these models are capable of evolving to include more realistic treatment of the "soft" solar wind-ionosphere interface, thus providing the possibility of a combined or coupled model of both the magnetotail/magnetosheath region and the ionopause/ionosphere. These models, and their future further-developed counterparts, will be of great value in the comparative study of the Venus and Mars solar wind interactions expected in the coming era of renewed Mars exploration.

I. INTRODUCTION

A. Background

Modeling the solar wind interaction with Venus presents a special challenge because it involves aspects of both magnetospheric and cometary solar wind interactions. As mentioned in the introductory chapter by Donahue and Russell, the solar wind induces currents in the planetary ionosphere that make it behave, in some respects, like an "impenetrable" closed magnetospheric obstacle. At the same time, heavy particles that form the planetary atmosphere can be ionized both in the surrounding solar wind and within the magnetosheath created by the obstacle. These heavy ions "mass-load" the plasma in these regions, thereby altering the flow and field properties. Moreover, the scale sizes of some of the pick-up ion gyroradii add kinetic influences to the solar wind interaction.

In this chapter we consider the various approaches that have been applied to the Venus-solar wind interaction to model its global characteristics. Many of these models were developed as either predictive tools or in response to measurements obtained by spacecraft. To maximize their realism, and in particular, to simulate the three-dimensional features of the solar wind interaction, they are necessarily numerical solutions. However, some have been adapted especially for comparisons with observations, with inputs and outputs designed to allow studies of how the interaction would appear along a spacecraft trajectory, or to accommodate changes for different interplanetary conditions. Most of the models are based on fluid approximations, wherein the solar wind (including in some cases the locally produced planetary ions) is treated by solving standard sets of fluid equations using finite difference methods on a spatial grid. However, a few treatments numerically solve the equations of motion for individual ions as a means of either determining the behavior of a minor (e.g., planetary) species, or of introducing ion kinetic effects.

In all cases it is assumed that an inner boundary exists at a highly conducting obstacle of either blunt body or spherical shape where the flow velocity and magnetic field become tangential to the surface. This presupposes that an effectively solid barrier is present to deflect the solar wind flow whether or not planetary ion pickup is significant in the interaction. Thus Venus models are unlike most purely cometary models which assume that only sources of heavy ions are present in the ambient flow. In some senses, the Venus models with planetary ion production can be considered as equivalent to cometary models with conducting obstacles at their centers. Of course the Venus ionosphere does not always behave so ideally in providing a sharp boundary between what can be considered solar wind (or magnetosheath) and the ionosphere proper. Here we address that lack of clear separation to only a minor extent in the discussion of ion kinetics. The details of the ionopause boundary behavior as well as the consequences of that boundary's sometimes diffusive nature are described in the chapter by Cravens et al.

As of this writing, most work on the global nature of the Venus–solar wind interaction involving models has made use of the gas dynamic model of Spreiter and Stahara (1980*a*,*b*) because of its relative simplicity, adaptability, and availability. For this reason, it is emphasized here. The descriptions of the recent, more physically comprehensive models are limited because they are generally still in the development and testing stage and have not yet been extensively probed or compared with observations.

B. Solar Wind at the Orbit of Venus

The solar wind flow parameters and planet size ultimately determine the appropriateness of the various simulation approaches. At the heliocentric distance of Venus, Luhmann et al. (1993) find the following median properties:

TABLE I
Median Properties at the Heliocentric Distance of Venus[a]

Density	~ 18 cm^{-3}	~22 cm^{-3}
Velocity	~400 km s^{-1}	~410 km s^{-1}
Ion temperature	~1 × 10^5 K	~1 × 10^5 K
Magnetic field	~12 nT	~10 nT
Parker Spiral angle	~38 deg	~35 deg
Dynamic pressure	~5 nPa	~6 nPa
Sonic Mach	~6.8	~7.0
Alfvén Mach	~7.0	~9.0
Magnetosonic Mach	~4.5	~5.5
Beta[b]	~1.5	

[a] Based on PVO measurements.
[b] Requires estimates of electron temperature.

In general, the solar cycle changes are modest. Because of conversion of the much greater flow energy to thermal energy at the bow shock, the thermal solar wind proton gyroradius of ~15 km near Venus can increase to 100s of km in the post-shock magnetosheath. However, it is again reduced (by ~50%) closer to the planet due to the compression of the field. Given the planetary radius of ~6050 km, this finite gyroradius motion causes only a small perturbation on the proton flow pattern around Venus. On the other hand, exospheric oxygen ions that are produced in the proton flow and accelerated by the solar wind convection electric field to solar wind speeds can have gyroradii that are a substantial fraction of a Venus radius.

II. GLOBAL MODELS

A. Gas Dynamic Models

1. Basic Model. The earliest and most extensively used global models of the Venus-solar wind interaction by Spreiter and coworkers (see, e.g.,

Spreiter et al. 1966,1970; Spreiter and Alksne 1969; Spreiter and Rizzi 1974; Spreiter and Stahara 1980*a*,*b*) considered the numerical solution, by finite difference methods, of the problem of hypersonic fluid or gas flow around an impenetrable blunt body. For this physical picture, the interaction is characterized by the formation of a bow shock that stands upstream of the obstacle where it serves to slow the flow to subsonic speeds prior to its divergence around the obstacle. Although these "magnetosheath" models do not address the physics of the wake region, they provide a means of analyzing the behavior of the dayside interaction in regions removed from the obstacle shadow. The equations that are solved:

continuity

$$\frac{\partial \rho}{\partial t} + \frac{\partial}{\partial x_k}(\rho v_k) = 0 \tag{1}$$

momentum

$$\rho \frac{\partial v_k}{\partial t} + \rho(\bar{v} \cdot \nabla) v_k + \frac{\partial p}{\partial x_k} = 0 \tag{2}$$

and energy

$$\frac{\partial \epsilon}{\partial t} + \frac{\partial}{\partial x_k}[(\epsilon + p) v_k] = 0 \tag{3}$$

where t is time, ρ is mass density, x_k a spatial coordinate, v_k the fluid velocity component along x_k, ϵ the total (internal plus kinetic) energy, and p the pressure given by the ideal gas law $p = \rho RT/m$ (related to the other variables by $p = (\gamma - 1)[\epsilon - \rho v^2/2]$ with γ the ratio of specific heats) are standards in fluid or gas dynamic theory (see, e.g., Spreiter et al. 1966). These have generally been solved for the Venus interaction case in conservative form using the cylindrical symmetry approximation with respect to the Venus–Sun line. The blunt-body shape of the obstacle is parameterized according to a value H/R_0, the atmosphere scale height (H) in obstacle nose radii (R_0). Shapes are obtained from the assumption of "Newtonian" pressure balance between the external solar wind ram pressure and an internal isothermal, spherically symmetric ionosphere with isotropic pressure obeying a hydrostatic law.

As mentioned above, the internal boundary condition of the numerical solution of these equations forces the normal component of the velocity to be zero on the blunt body. This is achieved by making the blunt body the inner boundary of the grid for the finite difference solutions. For the nose region portion of the solution, the outer boundary of the grid is located at an initial estimated position of the bow shock determined from an approximate formula. The appropriate jump conditions are applied at the bow shock discontinuity whose location is iteratively adjusted during the solution procedure until it converges to the actual shape. A sample grid is shown in Fig. 1. The spatial resolution in the inner cells is on the order of 0.01 R_0. An algorithm due to Beam and Warming (1978) allows the implicit solution of the unsteady Eqs. (1–3) in conservation form until a steady condition is achieved in the nose

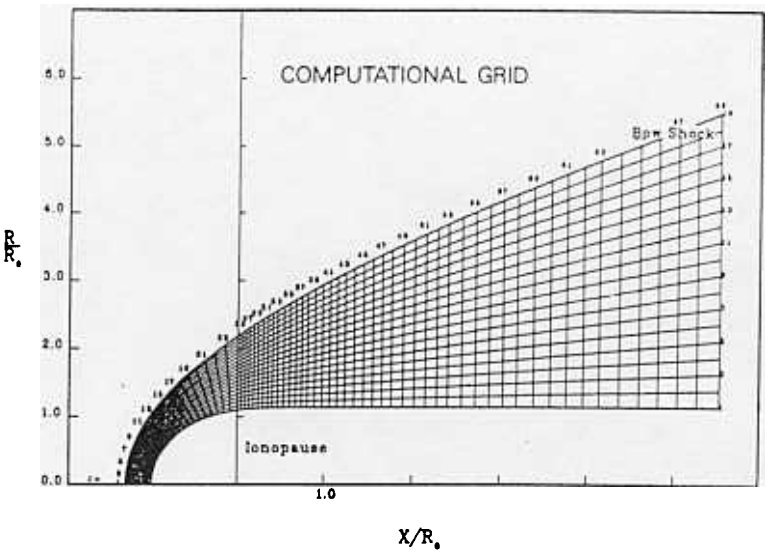

Figure 1. Computational grid used in Spreiter/Stahara gas dynamic models of the Venus magnetosheath (figure from Spreiter and Stahara 1992).

region. Downstream of this region, an explicit predictor-corrector scheme due to MacCormack (1969) is employed.

The only input parameters affecting the solution besides the obstacle shape are a (nominally sonic) Mach number and the ratio of specific heats γ. The resultant cylindrically symmetric, gas dynamic flow field variables (ρ, v, T), examples of which are given in Fig. 2, are normalized by the upstream values. As a consequence, they can be applied to a variety of upstream parameters following the initial solution as long as the assumed Mach number is taken into consideration. An interplanetary magnetic field of arbitrary strength and orientation can then be specified for the separate convected-field part of the gas dynamic model calculation.

The magnetic field $\bar{B}$ is assumed to be steady, frozen-in, and divergence-free, implying satisfaction of the two equations

$$\nabla \times (\bar{v} \times \bar{B}) = 0 \tag{4}$$

$$\nabla \cdot \bar{B} = 0 \tag{5}$$

but these are not solved using the usual finite difference methods. Instead, they are handled in a more computationally efficient way by making use of the known properties of the flow field and the magnetic field effectively to decompose the problem into the separate convection of the parallel (to the flow) and perpendicular contributions. The normalized parallel contribution

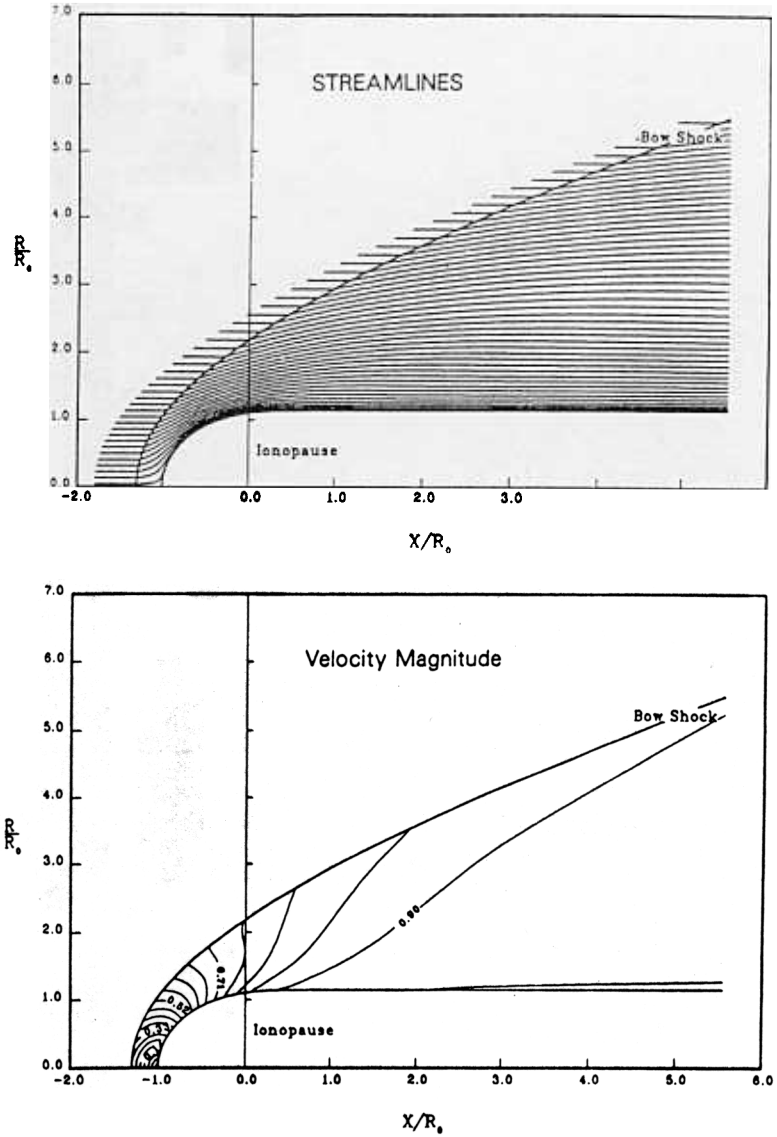

Figure 2. Samples of results from the (cylindrically symmetric) gas dynamic model (figure from Spreiter and Stahara 1992).

at any point follows the flow streamlines and has a magnitude given by

$$\left[\frac{B_{\text{local}}}{B_{\text{upstream}}}\right]_{\text{par}} = \frac{(\rho v)_{\text{local}}}{(\rho v)_{\text{upstream}}} \tag{6}$$

Similarly, the normalized contribution in the direction of the perpendicular

interplanetary field component is given by

$$\left[\frac{B_{\text{local}}}{B_{\text{upstream}}}\right]_{\text{perp}} = \frac{(\rho \nabla l)_{\text{local}}}{(\rho \nabla l)_{\text{upstream}}} \tag{7}$$

where ∇l is a "stretching factor" related to the change in the cross-stream tube distance between points originally aligned along the perpendicular direction upstream. The final orthogonal contribution (perpendicular to the plane of the upstream field) is

$$\left[\frac{B_{\text{local}}}{B_{\text{upstream}}}\right]_{\hat{n}} = \frac{(R\rho)_{\text{local}}}{(R\rho)_{\text{upstream}}}. \tag{8}$$

Here R is the radial cylindrical coordinate of the streamline through the point of interest and $\hat{n}$ is the unit vector normal to the plane containing the upstream field. The local orientation of the parallel field component in the magnetosheath is the local streamline orientation, while the local orientation of the perpendicular component lies parallel to a vector determined from analysis of the distortion of a small element of stream tube as it propagates through the magnetosheath. These contributions add vectorially to give the total field.

Examples of the field solution are reproduced in Fig. 3. Spreiter and Stahara (1980*b*) built a diagnostic routine into their code to "fly through" the gas dynamic model along a spacecraft orbit. This allows direct comparison of the model gas or plasma and field parameters with the Venus magnetosheath (sometimes called ionosheath) observations. Examples of magnetic field comparisons obtained by Luhmann et al. (1986) using Pioneer Venus Orbiter (PVO) magnetic field data are shown in Fig. 4. Russell et al. (1988) found that the best fit of the gas dynamic model bow shock to the observations could be achieved by using $\gamma = 5/3$, together with the magnetosonic (rather than the sonic) Mach number. Similarly, results of statistical comparisons with magnetic field data in the magnetosheath by T. L. Zhang et al. (1993) demonstrated that an obstacle size larger than the ionopause was required to match the bow shock and outer magnetosheath measurements. Both of these studies indicate that neglect of the magnetic field influence on the plasma inherent in the gas dynamic convected field model has significant consequences. The importance of the magnetic field influence could also have been concluded from the observation of the "magnetic barrier" (chapter by Donahue and Russell) in the inner magnetosheath wherein magnetic field pressure dominates. However, these problems can be approximately corrected for by manipulation of the obstacle size and Mach number. Even time variations in interplanetary conditions can be accommodated to a satisfying degree in the gas dynamic model by employing sequential steady state models (see, e.g., Spreiter and Stahara 1992). The one observation that motivated a real modification of the rather successful gas dynamic models was that the bow shock position varied with the solar cycle.

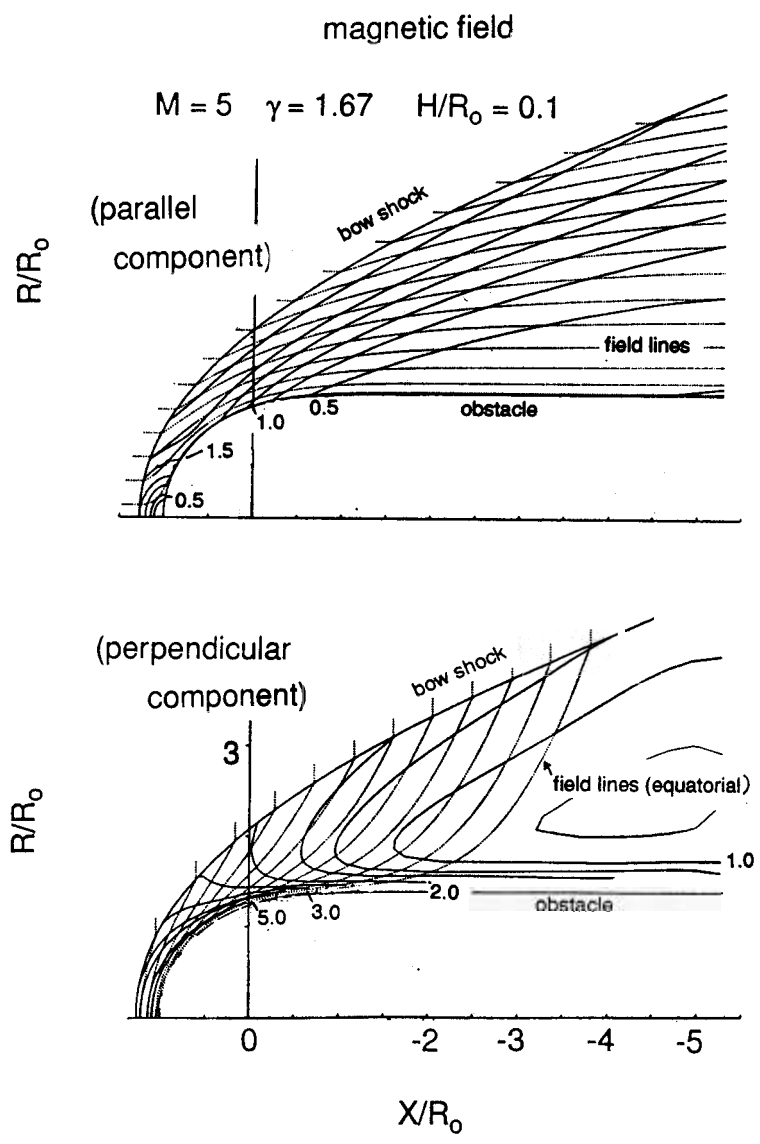

Figure 3. Magnetic field calculated by convecting a "frozen-in" interplanetary fiel through the gas dynamic model flow field in Fig. 2. The contours and field lines ar for the equatorial plane.

2. *Mass-Loaded Model.* Russell et al. (1988) and Zhang et al. (1990) showed that the average terminator radius of the bow shock was ~2.4 Venus radii (R_v) for solar maximum conditions, but only ~2.1 R_v for solar minimum conditions. Average solar wind parameters do not change sufficiently during

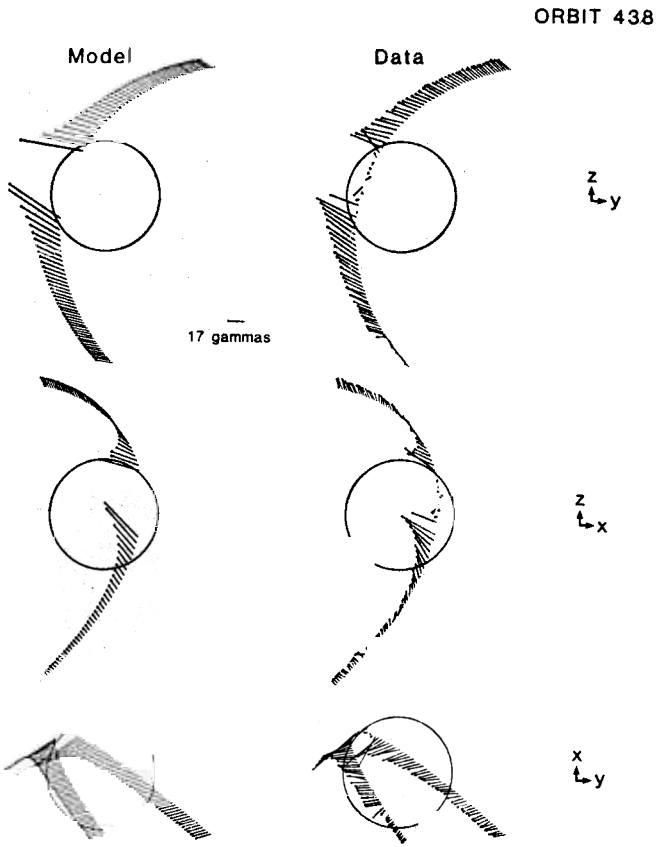

Figure 4. Comparison of magnetic field vectors computed from the gas dynamic model using the observed interplanetary magnetic field, with magnetometer measurements obtained along the orbit of the PVO. The views are (top) from the Sun, (center) in the noon-midnight meridian, and (bottom) as projected onto the plane of Venus' orbit (equivalent to the ecliptic) (figure from Luhmann et al. 1986).

the solar cycle to produce this variation, and so it was concluded that the shock movement must be related to a change in either the obstacle or in the rate of exospheric ion production in the magnetosheath and its effects. As mentioned in the overview chapter by Donahue and Russell, because the neutral atmosphere of Venus extends into the magnetosheath, substantial numbers of heavy (primarily atomic oxygen) ions are produced there by photoionization, impact ionization, or charge exchange (see, e.g., M. H. G. Zhang et al. 1993). The amount of photoionization increases at solar maximum as the solar EUV flux increases to ~2 to 4 times its solar minimum value. The EUV flux increase also enhances the upper atmosphere densities, and in particular affects the oxygen exosphere which depends on the ionospheric production rate for its source. To study a possible cause of this solar cycle

variation of the bow shock position, two gas dynamic models which include a comet-like source term, describing ion production appropriate for the Venus oxygen exosphere, were developed independently by Belotserkovskii et al. (1987) and Spreiter and Stahara (1992). The object of this modification was to determine whether the anticipated production of heavy planetary ions in the magnetosheath, or "mass-loading" would inflate the bow shock as observed. For simplicity, this source is assumed due to photoionization only and is treated as part of the single fluid, with its mass density production rate reflecting the fact that the newly produced ions are heavier than the solar wind hydrogen.

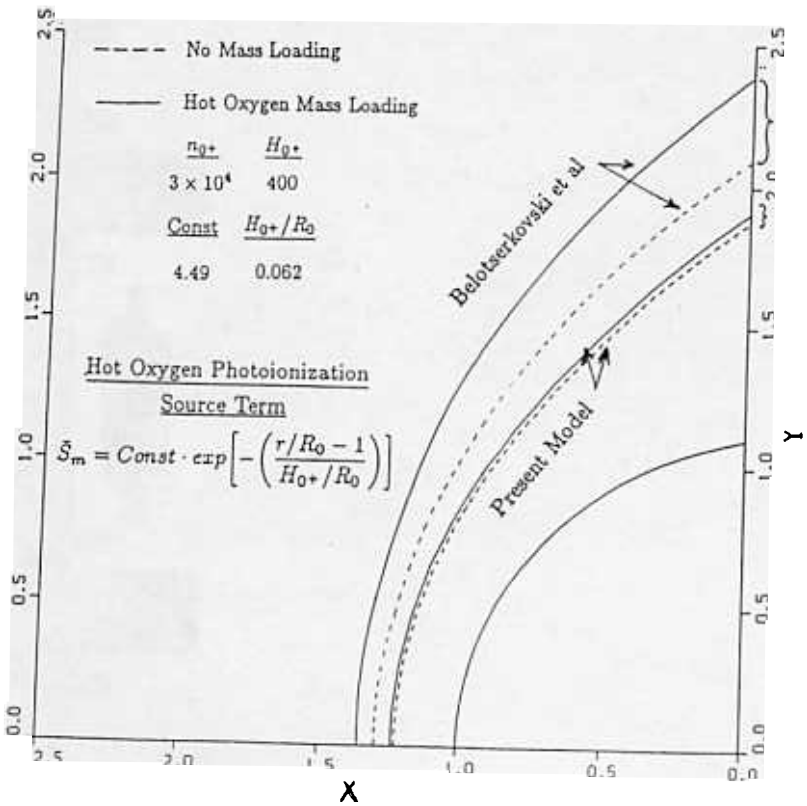

Figure 5. Comparison of gas dynamic model bow shocks with and without mass loading by oxygen exosphere ionization, as obtained by Belotserkovskii et al. (1987) and Spreiter and Stahara (1992). The form of the mass loading term is shown at left.

The atmospheric ion source term is added to the continuity equation (right-hand side of Eq. 1) only because the newly created photo-ions are presumed not to possess appreciable energy or momentum at the time of their creation (Spreiter and Stahara 1992; Belotserkovskii et al. 1987; see also

Breus et al. 1987). The form chosen

$$S = S_0 \exp\left[-\frac{(r - R_0)}{H_0}\right] \tag{9}$$

assumes the atmospheric density profile is a simple exponential. Here, S_0 is a constant proportional to the number density of neutral oxygen atoms at the obstacle nose position R_0($\sim 3 \times 10^4$ cm^{-3} times their mass) divided by the characteristic time for photo-ionization of atomic oxygen ($\sim 1 \times 10^6$ s at Venus at solar maximum), r is the radial distance from the center of the planet, and H_0 is the scale height of the oxygen exosphere (~400 km). As illustrated by Fig. 5, the results from the two models developed were strikingly different. Belotserkovskii et al. (1987) and Breus et al. (1987,1989) concluded that the expected rate of oxygen ion production could inflate the Venus bow shock to its observed solar maximum position, while Spreiter and Stahara (1992) found the same rate insufficient to produce any movement approaching the observed inflation. Moore et al. (1991*a*) modified Spreiter and Stahara's treatment by introducing an ionospheric obstacle shape that converged on the night side. This approach allowed the simulation of a rudimentary induced "magneto-tail." Based on both the amount of magnetic field draping in the modeled magnetotail and the bow shock position, Moore et al. (1991*a*) came to the same conclusion regarding the inability of these simple mass-loaded models to reproduce the shock position. Some possible origins of the contradictory results for similar approaches (albeit using different numerical methods to solve the gas dynamic equations) were discussed by Spreiter and Stahara (1992). We here adopt their conclusion that photo-ionization of the exosphere was insufficient to move the gas dynamic bow shock by the amount observed on PVO.

The apparent need for a stronger source term in the gas dynamic model can be interpreted in several ways. Provided that both the exospheric model (which has been verified with PVO ultraviolet spectrometer observations) and the photo-ionization rate are fairly accurate, possible additions to the apparent source could arise from: a thermospheric contribution with a smaller scale height at the lowest altitudes, or additional ionization mechanisms such as solar wind electron impact and charge exchange with solar wind protons (see, e.g., M. H. G. Zhang et al. 1993). Errors in the effective obstacle size or shape due to the neglected magnetic barrier, and magnetic field effects on the flow properties could also contribute to the inadequacy of the mass-loaded gas dynamic model predictions. The assumed "impenetrability" of the obstacle at solar minimum may also be violated. Finally, effects of the finite ion gyroradius, or the possibly inappropriate assumption that planetary photo-ions are adequately treated within the single fluid approximation, need to be considered.

The effects of the thermospheric contribution to the mass-loading, though not tested, were considered unlikely to provide the solution because these

effects should be confined to regions near the inner magnetosheath boundary. On the other hand, additional ionization mechanisms can enhance the mass-loading effects at higher altitudes. M. H. G. Zhang et al. (1993) suggest that, even at solar maximum, the contribution of solar wind electron impact may be twice as important as photo-ionization. They further show that its distribution is such as to raise substantially the oxygen ion production rate in the subsolar middle magnetosheath. Because the mass-loading rates in the gas dynamic models have not yet been altered to reflect this additional source, the extent to which it may solve the bow shock location problem remains to be determined. However, more recent numerical simulations allow some assessment of the magnetic field effects, as well as of the influence of ion gyroradius-scale physics.

B. Magnetohydrodynamic Models

In general, numerical magnetohydrodynamic (MHD) models involve finite-difference solutions of the same set of fluid equations as the gas dynamic models, but with the addition of magnetic force terms:

continuity

$$\frac{\partial \rho}{\partial t} + \nabla \cdot (\rho v) \quad 0 \tag{10}$$

momentum

$$\rho \frac{\partial \bar{v}}{\partial t} + \rho(\bar{v} \cdot \nabla)\bar{v} + \nabla p = \frac{1}{\mu}(\nabla \times \bar{B}) \times \bar{B} \tag{11}$$

energy

$$\frac{\partial \epsilon}{\partial t} + \nabla \cdot ((\epsilon + p)\bar{v}) = \frac{}{\mu}(\nabla \times \bar{B}) \cdot (\bar{v} \times \bar{B}). \tag{12}$$

In addition, they include self-consistent solution of a subset of the Maxwell equations in the forms:

Ampere's Law

$$\mu \bar{J} = \nabla \times \bar{B} \tag{13}$$

Faraday's Law

$$\frac{\partial \bar{B}}{\partial t} + \nabla \times \bar{E} = 0 \tag{14}$$

Induction Equation (frozen-field)

$$\bar{E} + \bar{v} \times \bar{B} = 0 \tag{15}$$

where $\bar{E}$ is the electric field and $\bar{J}$ is the current density. (The induction equation is derivable from the generalized Ohm's Law.) The divergence-free field condition, described by $\nabla \cdot \bar{B} = 0$, is also enforced in these models by various means.

Although there have been several MHD modeling efforts specifically for magnetosheaths, in the spirit of the gas dynamic models described above (see,

e.g., Wu 1992), we here look beyond these to consider others designed especially for the nonmagnetic planet-flow interactions including the wake region. Tanaka (1993), Cable and Steinolfson (1995), and DeZeeuw et al. (1996) independently solved the problem of hypermagnetosonic flow around a conducting sphere as a first approximation to the nonmagnetic planet interaction. Their computational methods differed significantly. DeZeeuw et al. used an adaptive grid, while Tanaka, and Cable and Steinolfson used a spherical grid with radial spacing increasing with distance from the planet. Moreover, Tanaka and DeZeeuw et al. used monotone upwind scalar-conservation law (MUSCL) algorithms (see Gombosi et al. [1994] for a further description and references), while Cable and Steinolfson used a form of Lax-Wendroff operator with a smoothing term to inhibit numerical instabilities. Their maximum spatial resolution also differs. Near the conducting sphere (of radius R_v), Tanaka worked with a grid spacing of .1 R_v, while Cable and Steinolfson imposed 0.017 R_v spacing. The near-planet resolution in the DeZeeuw et al. model is 0.063 R_v. The physical parameters of their external (solar wind) flows are, respectively, (magnetosonic) Mach numbers of ~10, 3, 4 and plasma betas (thermal pressure/magnetic pressure) of 1.5, 0.6, 1.8 (or 6.0) for Cable and Steinolfson, DeZeeuw et al., and Tanaka. The interplanetary magnetic field orientation in the Tanaka model is perpendicular to the upstream velocity, in the Cable and Steinolfson model three different interplanetary field "cone" angles of 0°, 45°, and 90° are adopted, and in the DeZeeuw et al. model the upstream field is flow aligned. Because the results of each model are displayed somewhat differently, they are difficult to compare in any detail. However, some major features can be noted.

All of the models show upstream fast mode bow shocks with shock jumps in agreement with the Rankine Hugoniot relations. The terminator-to-nose radius ratios for the bow shocks are smaller by ~0.1 than the observed value of ~1.67 (Zhang et al. 1990) for the Tanaka (1993) and Cable and Steinolfson (1995) models, but larger for the DeZeeuw et al. (1996) model. The first two authors note that neglecting the the thickness of the ionosphere as part of the obstacle can cause their discrepancies. Cable and Steinolfson (1995) find that the quasi-parallel bow shocks are closer to the sphere than the quasi-perpendicular bow shocks. Pole–equator differences that have been observed in the bow shock radius in association with larger field cone angles (Russell et al. 1988) are found in the model results of both Tanaka (1993) and Cable and Steinolfson (1995). However, the degree of elongation in the polar directions (apparently produced by fast-mode wave speed differences in the polar and equatorial shock field and flow geometries) seems weaker than that derived from the measurements (~5% vs ~10%).

All of the models also show a density depletion in the low altitude nightside wake. In the cases where a perpendicular component of the interplanetary magnetic field is present, a magnetic barrier forms against the dayside obstacle, and an induced magnetotail connected to this barrier appears in the wake to the lowest altitudes modeled. Figure 6 shows the global field line config-

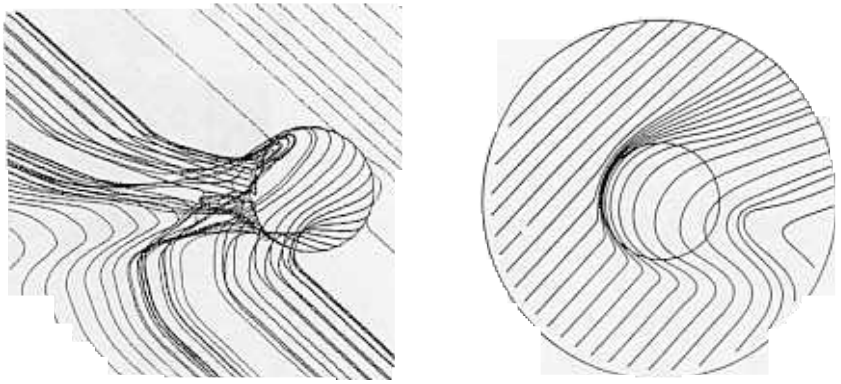

Figure 6. Draped magnetic field lines produced in the MHD simulations of the solar wind interaction with a conducting sphere carried out by Tanaka (1993) for perpendicular interplanetary magnetic field (left) and by Cable and Steinolfson (1995) for a 45° orientation (right). The latter is of selected field lines above the equatorial plane, projected down onto that plane.

uration from Tanaka (1993) for perpendicular upstream field and from Cable and Steinolfson (1995) for the 45° field. These configurations agree with general expectations based on the analysis of PVO magnetometer observations from solar maximum (see, e.g., the review by Luhmann 1986). A pressure maximum that occurs in the model between the magnetotail lobes is identified as a central plasma sheet. Both the Tanaka (1993) and Cable and Steinolfson (1995) results (for 45° and 90° cone angles) show accelerated "jets" of flow from the terminator regions where the magnetic field is sharply draped and undergoes a change of sign in its sunward–anti-sunward component. Indeed, the equatorial and meridional flow parameter contrasts, illustrated by Fig. 7, indicate that substantial asymmetries are present in the average interaction at Venus. Tanaka (1993) and Cable and Steinolfson (1995) also both found that the induced magnetotail lobes in their models appear weaker than in observations, possibly due to neglect of the atmosphere or ionosphere and/or mass-loading physics. Cable and Steinolfson moreover find reconnection of the low-altitude wake fields occurring in their model, although their numerical resistivity plays a role. Figures 8 and 9 show the magnetic field for the contrasting case of a precisely flow-aligned (radial) upstream field in which no traditional induced magnetotail is formed. The wake seems to contain weak vortices in both the flow and field (Fig. 8). This wake structure in fact shows good agreement with observations (Fig. 9), although the steady radial interplanetary field situation is rare. It is interesting that Tanaka (1993) also found indications of wake vortices in the magnetic equatorial region of their solution, but these did not manifest themselves so clearly in the presence of the induced magnetotail.

Overall, these models show considerable promise for probing the physics

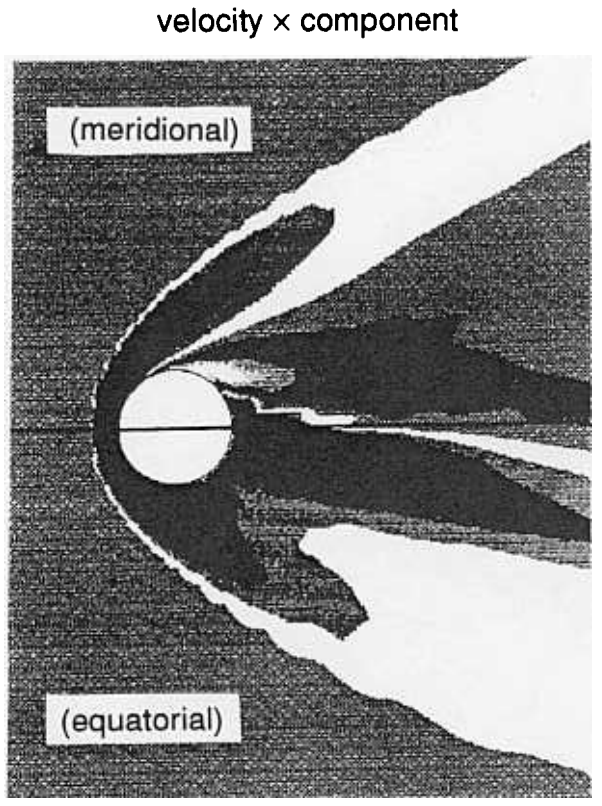

Figure 7. Contours of fluid velocity in the meridional (top) and equatorial (bottom) planes from the Tanaka (1993) global MHD simulation.

of the induced magnetotail formation and the influence of both magnetic forces and mass-loading on the solar wind interaction with Venus. They have yet to be fully examined and exploited. At the same time, because of their isotropic "fluid" nature, they will not by themselves help us to understand details related to the effects of ion kinetics in the solar wind interaction with Venus.

C. Test Particle Models

Test particle methods, in which the equation of motion is solved for single particles (usually ions) in prescribed field configurations, have been applied to model the global characteristics of planetary pick-up ions around Venus. The large gyroradii expected for heavy (e.g., oxygen) pick-up ions relative to the subsolar interaction region and planetary radius scales were first noted by both Wallis (1972) and Cloutier et al. (1974) at an early stage in the investigation of the Venus–solar wind interaction. At that time, test particle approaches were used (see, e.g., Cloutier et al. 1974) to illustrate the asymmetry of the ion wake that would result from impact of exospheric pick-up ions on the

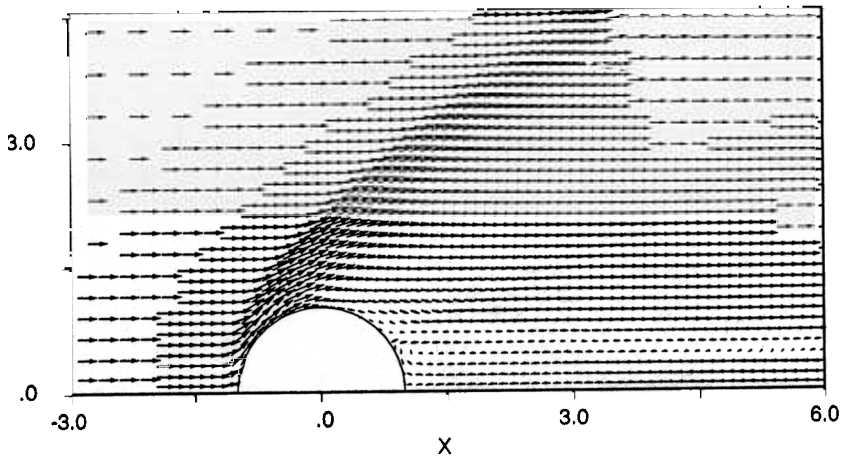

Figure 8. Magnetic field vectors in the wake of the flow-aligned field global MHD simulation by DeZeeuw et al. (1996). No classical induced magnetotail forms in this situation.

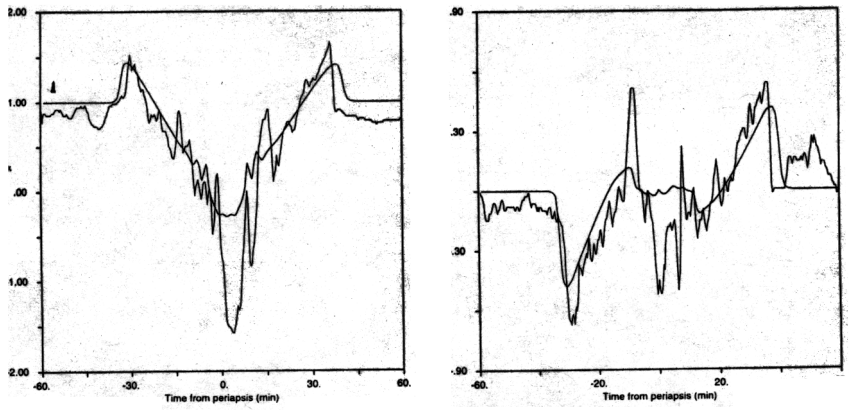

Figure 9. Comparison of some PVO magnetometer observations in the wake of Venus during a period of radial interplanetary field with the simulated field in the DeZeeuw et al. (1996) model.

dayside ionopause. The underlying field models in these early studies were highly simplified because of the limited computational capabilities available.

More sophisticated test particle models have since been constructed that make use of the results from the numerical models described above. These were in part motivated by the observations from the PVO (see, e.g., Phillips et al. 1987) which indicated first order agreement of the fluid model flows and fields with the actual situation, but required information outside of the framework of those models for interpretation of other data. For example,

Fig. 10 illustrates the general behavior of singly ionized oxygen (O^+) pick-up ions, which are "born" with negligible initial velocities in the dayside gas dynamic model of the Venus magnetosheath. The trajectories are computed by numerically solving the ion equation of motion,

$$\bar{a} = (q/m)(\bar{E} + \bar{V} \times \bar{B}) \tag{16}$$

where $\bar{V}$ is the particle velocity, $\bar{a}$ is its acceleration, and q/m is the charge to mass ratio. The fluid models provide the description of $\bar{B}$ and the convection electric field $\bar{E} = -\bar{v} \times \bar{B}$ where $\bar{v}$ is the fluid bulk velocity. Phillips et al. (1987) used such trajectories to estimate the pick-up ion current perturbation of the magnetosheath field.

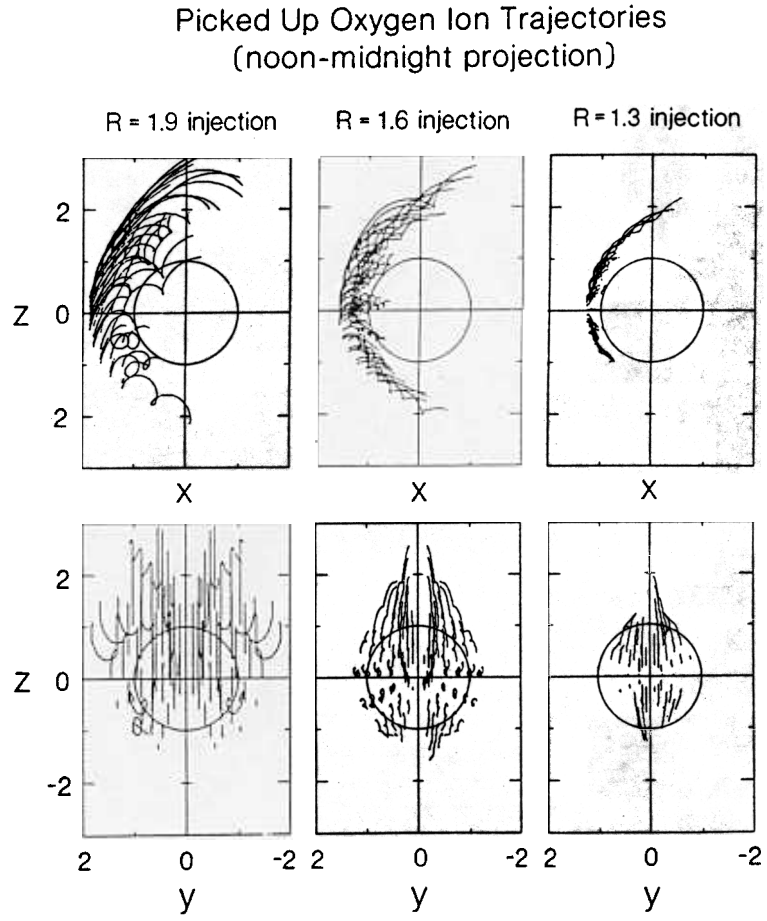

Figure 10. Picked up oxygen ion trajectories calculated using O^+ test particles in the Spreiter/Stahara gas dynamic magnetosheath model with the convected field.

Luhmann and Kozyra (1991) used a similar test particle model of the exospheric ion pickup to evaluate the flux of re-entering pick-up ions and to study their aeronomical effects; however, much of the interest in these ions relates to their role in induced magnetotail formation, a region not generally addressable with the blunt-body gas dynamic models. The modification introduced by Moore et al. (1991*a*), in which closure of the blunt-obstacle surface on the night side of the planet was assumed, provided one approximate solution. Moore et al. launched O^+ ions in the dayside magnetosheath, weighting them according to their altitude of origin using an exospheric model, to obtain spatial distributions and energy spectra in the wake region. Some of their ion trajectories are reproduced in Fig. 11. Based on this model, Moore et al. concluded that there must be a fluid-like mass addition at low altitudes that remains confined to the vicinity of the obstacle boundary, plus a high-energy, high-altitude component that exhibits an asymmetry controlled by the direction of the solar wind electric field $\bar{E} = -\bar{v} \times \bar{B}$. They further concluded that much of the lower energy, low-altitude-origin component was undetectable with the Pioneer Venus instruments.

Other test particle calculations by Luhmann (1993) used a comet tail model to represent the fields in the space occupied by the blunt body in the gas dynamic magnetosheath model. That construction, while implicitly suffering from a discontinuity in the flow and field at the blunt body boundary, is fairly consistent with PVO magnetometer measurements in the low-altitude wake. Equatorial field lines for this alternative magnetotail model are shown in Fig. 12. In this case, The self-consistent, anti-sunward flow underlying the comet-tail field lines determines the convection electric field in the pick-up ion equation of motion. Ionospheric particles launched tailward from the terminator within the space occupied by the comet tail model generally remain there to large distances. In particular, when the gravitational force is added to the equation of motion and the background velocity at the launch site (altitudes below ~1500 km) is assumed to be low (several tens of km s^{-1}), the pick-up ions obtain energies in the tens of eV range and form spatial patterns in the low-altitude wake reminiscent of the Venus ionospheric "tail rays" (Brace et al. 1987). Figures 13 and 14 show, respectively, examples of the low-altitude pick-up O^+ trajectories obtained by Luhmann (1993) and cross sections of the tail-ray-like structures. The behavior of these pick-up ions results from the combination of a low pick-up velocity, pickup where there is a substantial angle between the local magnetic field and underlying flow (e.g., "draping"), and the narrowness of the assumed low-altitude terminator source region. Recent work with analogous models to greater downstream distances further suggests that the observed, more energetic (~keV) ions observed at the PVO apoapsis of ~12 R_v (see, e.g., Moore et al. 1990) may be the distant wake counterparts of the ionospheric tail rays instead of the population of high-altitude exospheric origin. Indeed, the latter may produce fluxes too weak to be observed on PVO.

A great advantage of test particle models is their flexibility, which is

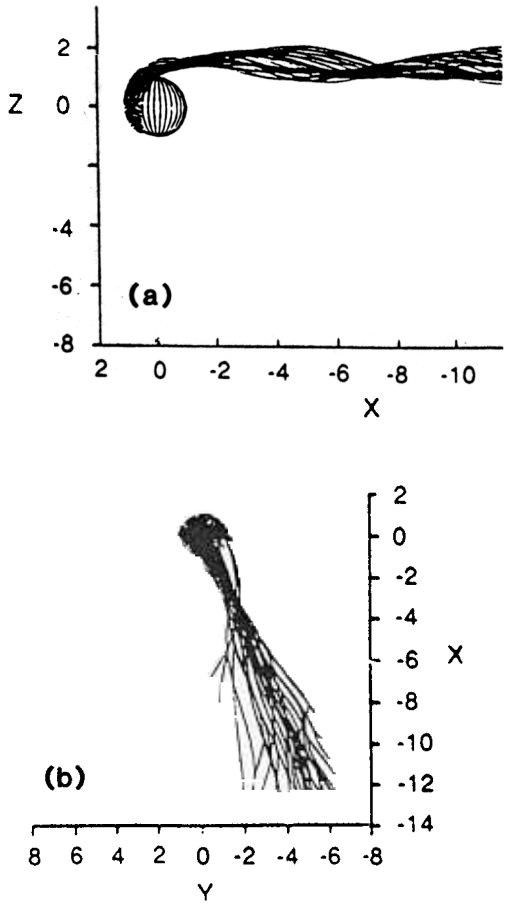

Figure 11. O^+ ion trajectories initiated on the day side of Venus and subjected to the modified gas dynamic model fields of Moore et al. (1990). The Parker spiral interplanetary field is assumed. (a) Meridional view. (b) Equatorial projection.

limited mainly by the availability of suitable background field and flow models. Provided that enough is known or can be assumed about the underlying "fluid" behavior, one can freely place particles of any mass, charge, and initial velocity, and characterize their subsequent behavior. However, these models can be criticized for their lack of physical self-consistency, which limits their usefulness for some applications.

D. Hybrid Models

The lack of self-consistency in test particle models largely vanishes in global hybrid models such as those developed by Brecht (1990), Moore et al. (1991*b*), and Brecht and Ferrante (1991), although adequate spatial resolution and ion statistics in these models comes at great computational cost. In typical cases,

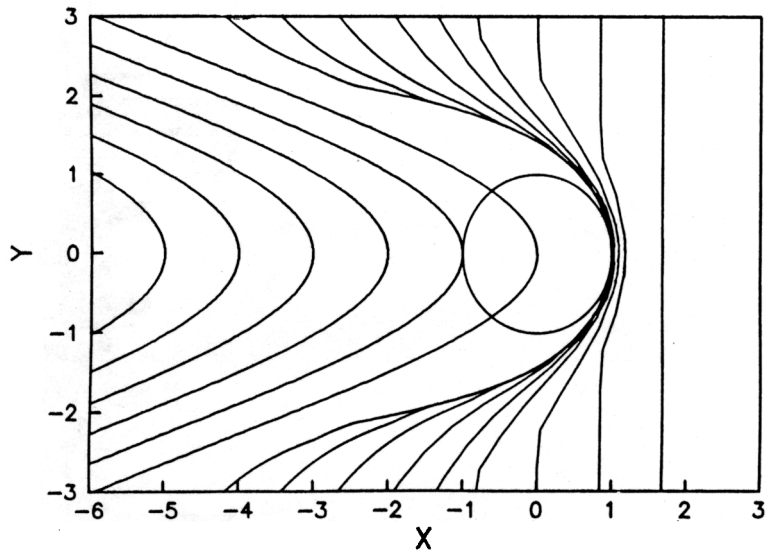

Figure 12. Modification introduced to the classical gas dynamic magnetosheath model by Luhmann (1993) to describe the fields in the wake.

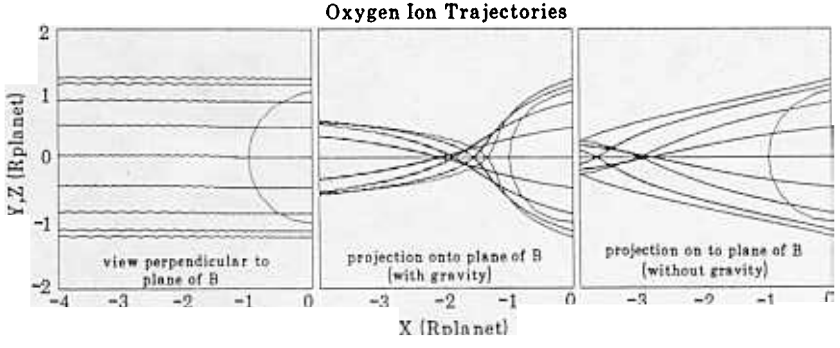

Figure 13. Low-energy O^+ ion trajectories obtained with a field of the form shown in Fig. 12. These ions were launched in a ring around the terminator at altitudes inside the gas dynamic magnetosheath model obstacle. Thus they move only in the comet-like "magnetotail" model.

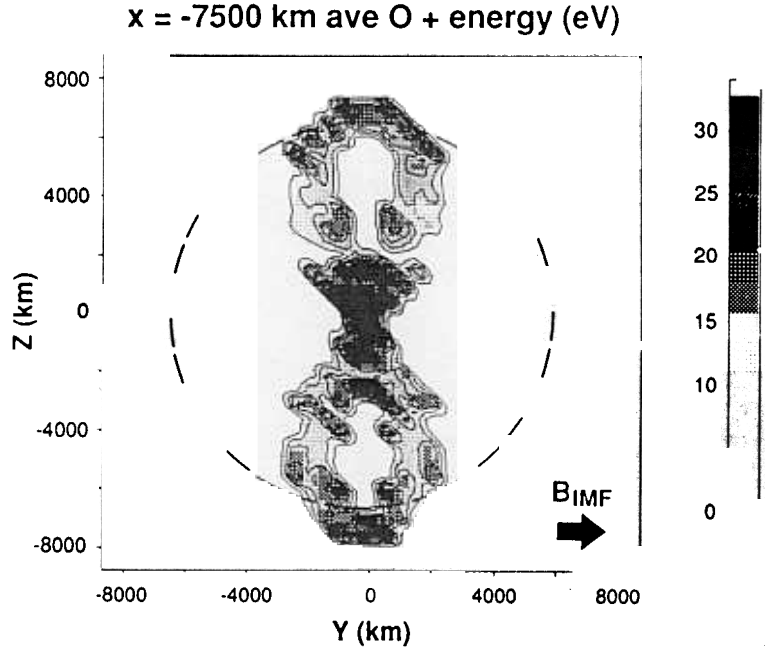

Figure 14. "Tail ray" structure resulting from an assumed low-altitude terminator source and the comet-like tail field model.

the ion equation of motion (Eq. 16) is solved for millions of particles to obtain the ion distribution function (and hence density and bulk velocity), while the electrons are treated as a massless fluid. Quasi-neutrality is assumed in the equations solved. The momentum equation for the electron fluid, with a resistive term $\eta \bar{J}$ added to $\bar{E}$ to allow some diffusion and dissipation of the magnetic fields, is solved for the electric field:

$$\bar{E} = \bar{v}_e \times \bar{B} - \frac{1}{qn}\nabla p_e + \eta \bar{J} \tag{17}$$

where $\bar{v}_e$ is the electron fluid bulk velocity, n is the number density, η is the resistivity, and J is the current density. Faraday's Law (Eq. 14) is used to determine the self-consistent magnetic fields between steps of particle distribution advancement in time. Details concerning the numerical methods can be found in the paper by Brecht and Thomas (1988). High-frequency ($\gtrsim \omega_{ce}$, the electron gyrofrequency) electromagnetic waves are excluded by the assumption of zero electron mass, and quasi-neutrality. However, electromagnetic waves such as ion cyclotron, mirror modes, left-hand modes, and some electron whistlers, in addition to MHD waves are simulated, and can be driven physically by anisotropies that develop in the ion distribution functions.

Mass-loading is accommodated self-consistently in the hybrid models simply by introducing new ions with different masses heavier than protons

at the appropriate spatial locations and rates to simulate their "birth" by ionization of the parent exospheric neutrals (Moore et al. 1991*b*). To date, these models have not included charge exchange or impact ionization collision processes. Moore et al. (1991*b*) considered the dayside interaction only, injecting O^+ ions at zero velocities at a rate that reflects the exospheric oxygen photo-production of 5×10^{24} s^{-1} for solar maximum. The assumed upstream solar wind density and velocity were 10 cm^{-3} and 500 km s^{-1}, respectively, and the interplanetary magnetic field of 12 nT was oriented 45° from the upstream flow direction. Solar wind ions were assumed cold, but solar wind electrons had 50 eV temperatures. The Alfvén, sonic, and fast Mach numbers were 8.5, 5.6, and 5.0. Because of computational limitations, Moore et al. used a spherical planetary obstacle about half the size of Venus, and then adopted an effective oxygen exosphere scale height and oxygen mass equal to half their actual values to obtain the appropriate relative scaling. The grid or cell size for the fluid solution, defining the model resolution, was $102 \times 360 \times 360$ km^3. Trajectories of some protons and oxygen ions from their simulation are reproduced in Fig. 15. As was also noted by Brecht (1990), asymmetries in apparent flow around the spherical obstacle in the hybrid model also occur for the solar wind protons, although they are exaggerated here due to the small obstacle assumed. Essentially all of the solar wind protons are diverted around the obstacle by a dayside magnetic barrier that forms as in the MHD models, except that in this case it is asymmetrical like the flow. Hall current associated magnetic gradient drifts in the barrier produce the asymmetric deflections. The oxygen ions, with their larger gyroradii, tend to impact the obstacle where they are removed from the simulation. Moore et al. (1991*b*) found that a realistic O^+ production rate did not significantly affect their hybrid model bow shock position. However, increasing the O^+ production rate by a factor of 5 caused an outward displacement on the order of what is observed between solar minimum and maximum on PVO. They also suggested that part of the explanation for the observed degree of ellipticity in the shock cross section may be that the quasi-parallel shock forms closer to the planet than the quasi-perpendicular shock by an amount in excess of that predicted from MHD alone.

Brecht and Ferrante (1991) produced a higher spatial resolution version of the three-dimensional hybrid model, (~50–100 km cell sizes), but were consequently restricted to just the nose region of the interaction. Like Moore et al. (1991*b*), they showed that the concept of a stagnation streamline does not apply in the hybrid model, and that the dayside magnetic barrier exhibits Hall-current induced asymmetries. They did not consider the effects of mass loading by O^+ ions, but experimented with the solar wind proton gyroradius to planet scaling and concluded that the spatial resolution in the Moore et al. (1991*b*) simulation was probably too coarse to reproduce the actual shock location. Of course, the position of their own subsolar bow shock was compromised by the limited part of the obstacle that was considered. These authors also tried hemispherical obstacles, which seemed to produce subsolar bow shock positions in basic agreement with observations. They more recently extended their model, at lower spatial resolution, to a full sphere for the scaling of Mars in the solar wind (1995, unpublished manuscript). A fully global hybrid simulation has yet to be carried out for Venus. See the CD-ROM for animations CDP1C2M1 and CDP1C2M2.

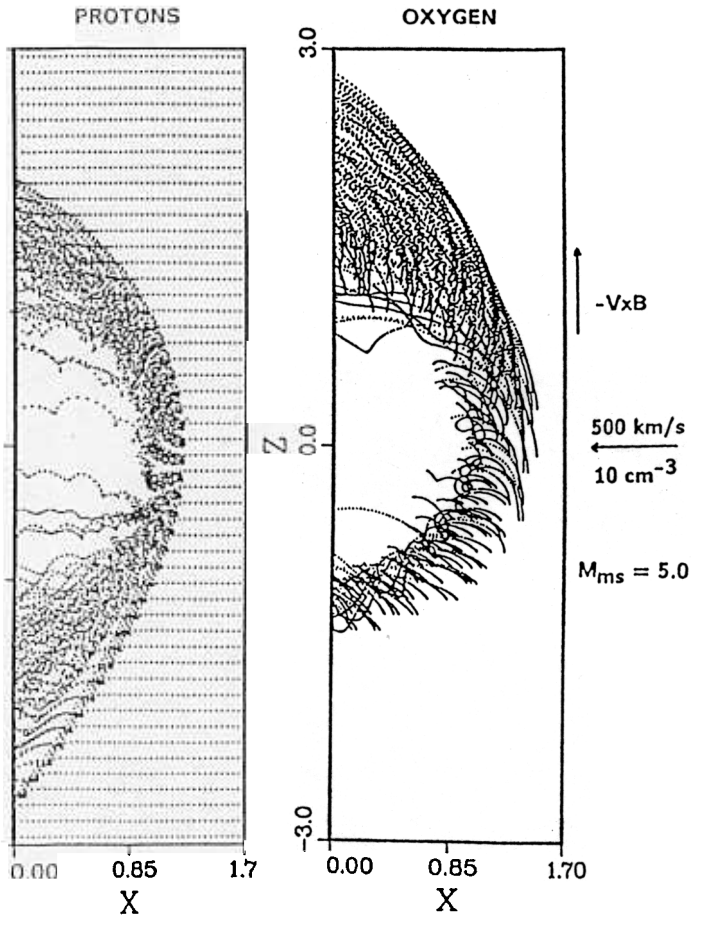

Figure 15. Dayside solar wind proton and exospheric O^+ ion trajectories from the hybrid model treatment of the solar wind interaction by Moore et al. (1991*b*).

In general, the hybrid models show considerable structure in their plasmas and fields, some of which may be noise introduced by the numerical methods and the finite numbers of ions, but some of which is physical. Examples of altitude profiles of dayside magnetosheath magnetic field and density from a hemispherical simulation of Brecht and Ferrante (1991) are shown in Fig. 16. Because this structure changes from time step to time step, such

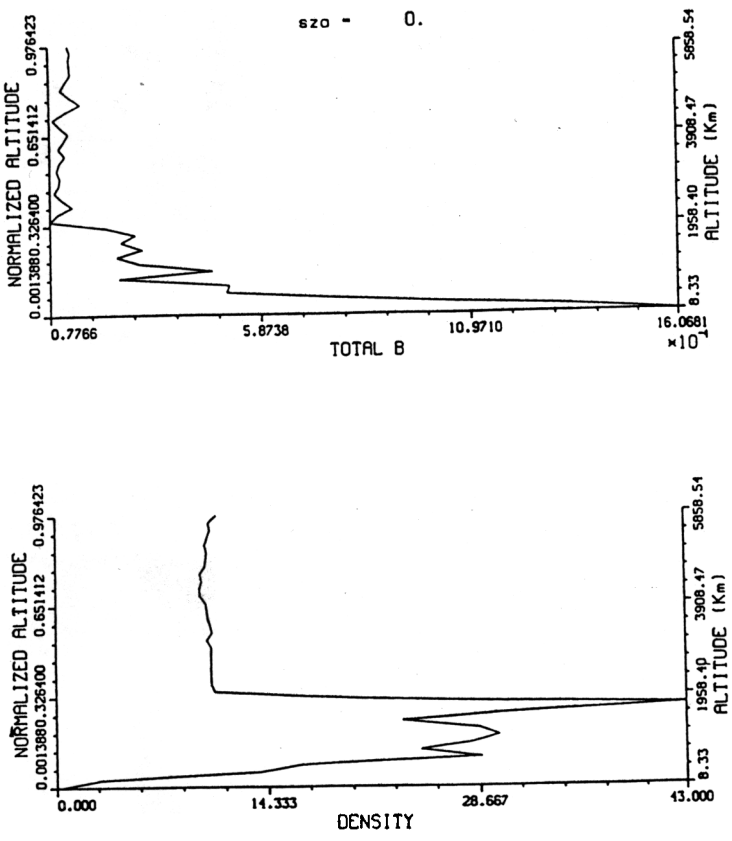

Figure 16. Simulated altitude profiles of the dayside magnetosheath magnetic field and proton density from the hybrid model of Brecht and Ferrante (1991). This model did not include O^+ ion effects.

displays must be regarded as "snapshots" from one instant. The amount of structure diminishes with averaging on the time scale of most observational data intervals.

Moore et al. (1991*b*) also experimented with the effect of finite obstacle conductivity. They found that the shock standoff distance is reduced if the magnetic fields are allowed to diffuse into the obstacle. Because this situation resembles, in some respects, what happens when the dayside ionosphere becomes magnetized (see the chapter by Cravens et al.), their simulations may have the potential of explaining the solar minimum and high solar wind dynamic pressure scenarios. Indeed, Zhang et al. (1990) inferred from bow shock observations and the gas dynamic model that the effective solar minimum subsolar obstacle would have to be located at or below the planet's surface. Instead, the explanation may be that the ionospheric obstacle becomes a less perfect conductor than at solar maximum. A further implication

is that if the magnetic fields induced in the obstacle fail to set up an effective magnetic barrier, some of the solar wind particles will be absorbed. Clearly, much can be learned by experimenting with these state-of-the-art global self-consistent simulations including ion kinetics.

III. CONCLUSIONS

Each type of model described above makes unique contributions to the study of the solar wind interaction with Venus. The gas dynamic model provides a flexible tool for analyzing the dayside magnetosheath field configuration for a variety of interplanetary field orientations, and for carrying out first order studies of the bow shock position and the effects of planetary ion addition to the solar wind plasma (mass loading). The MHD models on average have poorer spatial resolution than the gas dynamic models, but they include the physics pertinent to the formation of the magnetic barrier and its extension into the wake. They also allow the study of flow interaction asymmetries introduced by the magnetic forces. Both types of fluid models provide background field and flow descriptions that can be used for test particle analyses of the behavior of the planetary pick-up ions. The most physically complete but computationally restrictive type of model is of course the global hybrid model, which includes both the MHD and ion kinetic effects as well as certain wave modes and Hall currents. This last model has the potential for explaining all of the features seen in the fluid and test particle models, including the bow shock, induced magnetotail, and pick-up ion attributes and consequences, with modifications (e.g., asymmetries) introduced by anisotropic ion distributions and finite ion gyroradii. However, it is not yet practical to "experiment" extensively with such models. While the available space does not permit discussion of all of the details of the various global model results, the above sampling illustrates the wealth of insights that can be gained from such simulations. Of course, the models' various advantages and shortcomings need to be considered before using them for the interpretation of observations or prediction of expected features.

As computational capabilities improve and become more accessible, it is easy to envision how global simulations may be utilized. Processes like charge exchange and impact ionization interactions between solar wind particles and exospheric neutrals can be incorporated into both fluid and hybrid models in order to test their individual effects. The boundary condition at the obstacle may be relaxed to allow not only diffusion of the magnetic field and absorption of solar wind plasma, but also active pressure-balance adjustment of a realistic ionosphere. This will allow better assessment of solar cycle and evolutionary time scale changes, and give indications of the induced magnetic fields at the planet surface. Time-dependent interplanetary conditions can be assumed in order to examine the responses of the simulations to various solar wind structures such as tangential or rotational discontinuities in the interplanetary field, and interplanetary shocks. Indeed, because no space physics missions

to Venus are planned in the foreseeable future, much of our progress in further understanding the solar wind interaction and its consequences may be determined by these computational experiments. Comparisons with new observations from Mars, and applications of these models to that body, will also provide further understanding and discoveries relating to Venus. Thus with "bootstrapping" our knowledge should continue to grow in spite of the current outlook for *in-situ* measurements. Future generations who finally return to Venus exploration can benefit significantly from the on-going efforts described here, as our visions of near-Venus space and the global attributes and effects of the solar wind interaction with Venus' atmosphere become more complete.

REFERENCES

Beam, R. M., and Warming, R. F. 1978. An implicit factored scheme for the compressible Navier-Stokes equations. *AIAA J.* 16:393–402.

Belotserkovskii, O. M., et al. 1987. The effect of the hot oxygen corona on the interaction of the solar wind with Venus. *Geophys. Res. Lett.* 14:503–506.

Brace, L. H., et al. 1987. The ionotail of Venus: Its configuration and evidence for ion escape. *J. Geophys. Res.* 92:15–26.

Brecht, S. H. 1990. Magnetic asymmetries of unmagnetized planets. *Geophys. Res. Lett.* 17:1243–1246.

Brecht, S. H., and Ferrante, J. R. 1991. Global hybrid simulation of unmagnetized planets: Comparison of Venus and Mars. *J. Geophys. Res.* 96:11209–11220.

Brecht, S. H., and Thomas, V. A. 1988. Multidimensional simulations using hybrid particle codes. *Comput. Phys. Comm.* 48:135–143.

Breus, T. K., Krymskii, A. M., and Mitnitskii, V. Ya. 1987. Interaction of mass-loaded solar wind flow with a blunt body. *Planet. Space Sci.* 35:1221–1227.

Breus, T. K., Bauer, S. J., Krymskii, A. M., and Mitnitskii, V. Ya. 1989. Mass loading in the solar wind interaction with Venus and Mars. *J. Geophys. Res.* 94:2375–2382.

Cable, S., and Steinolfson, R. S. 1995. Three dimensional MHD simulations of the interaction between Venus and the solar wind. *J. Geophys. Res.* 100:21645–21658.

Cloutier, P. A., Daniell, R. E., and Butler, D. M. 1974. Atmospheric ion wakes of Venus and Mars in the solar wind. *Planet. Space Sci.* 22:967–990.

DeZeeuw, D. L., et al. 1996. A new axisymmetric MHD model of the interaction of the solar wind with Venus. *J. Geophys. Res.* 101:4547–4556.

Gombosi, T. I., Powell, K. G., and DeZeeuw, D. L. 1994. Axisymmetric modeling of cometary mass loading on an adaptive refined grid: MHD results. *J. Geophys. Res.* 99:21525–21540.

Luhmann, J. G. 1986. The solar wind interaction with Venus. *Space Sci. Rev.* 44:241–306.

Luhmann, J. G. 1993. A model of the ionospheric tail rays of Venus. *J. Geophys. Res.* 98:17615–17621.

Luhmann, J. G., and Kozyra, J. U. 1991. Dayside pickup oxygen ion precipitation at Venus and Mars: Spatial distributions, energy deposition and consequences. *J. Geophys. Res.* 96:5457–5467.

Luhmann, J. G., et al. 1986. A gas dynamic magnetosheath field model for unsteady interplanetary fields: Application to the solar wind interaction with Venus. *J. Geophys. Res.* 91:3001–3010.

Luhmann, J. G., et al. 1993. Solar cycle 21 effects on the interplanetary magnetic field and related parameters at 0.7 and 1.0 AU. *J. Geophys. Res.* 98:5559–5572.

MacCormack, R. W. 1969. The Effect of Viscosity in Hypervelocity Impact Cratering. AIAA Paper 69-354.

Moore, K. R., McComas, D. J., Russell, C. T., and Mihalov, J. D. 1990. A statistical study of ions and magnetic fields in the Venus magnetotail. *J. Geophys. Res.* 95:12005–12018.

Moore, K. R., McComas, D. J., Russell, C. T., Stahara, S. S., and Spreiter, J. R. 1991*a*. Gas dynamic modeling of the Venus magnetotail. *J. Geophys. Res.* 96:5667–5681.

Moore, K. R., Thomas, V. A., and McComas, D. J. 1991*b*. Global hybrid simulation of the solar wind interaction with the dayside of Venus. *J. Geophys. Res.* 96:7779–7791.

Phillips, J. L., Luhmann, J. G., Russell, C. T., and Moore, K. R. 1987. Finite Larmor radius effect on ion pickup at Venus. *J. Geophys. Res.* 92:9920–9930.

Russell, C. T., et al. 1988. Solar and interplanetary control of the location of the Venus bow shock. *J. Geophys. Res.* 93:5461–5469.

Spreiter, J. R., and Alksne, A. Y. 1969. Plasma flow around the magnetosphere. *Rev. Geophys.* 1:11–50.

Spreiter, J. R., and Rizzi, A. W. 1974. Aligned magnetohydrodynamic solution for solar wind flow past the Earth's magnetosphere. *Acta Astronaut.* 1:15–55.

Spreiter, J. R., and Stahara, S. S. 1980*a*. A new predictive model for determining solar wind-terrestrial planet interactions. *J. Geophys. Res.* 85:6769–6777.

Spreiter, J. R., and Stahara, S. S. 1980*b*. Solar wind flow past Venus: Theory and comparisons. *J. Geophys. Res.* 85:7715–7738.

Spreiter, J. R., and Stahara, S. S. 1992. Computer modeling of solar wind interaction with Venus and Mars. In *Venus and Mars: Atmospheres, Ionospheres and Solar Wind Interactions*, eds. J. G. Luhmann, M. Tatrallyay and R. O. Pepin (Washington, D. C.: American Geophysical Union), pp. 345–386.

Spreiter, J. R., Summers, A. L., and Alksne, A. Y. 1966. Hydromagnetic flow around the magnetosphere. *Planet. Space Sci.* 14:223–253.

Spreiter, J. R., Summers, A. L., and Rizzi, A. W. 1970. Solar wind flow past nonmagnetic planets—Venus and Mars. *Planet. Space Sci.* 18:1281–1299.

Tanaka, T. 1993. Configurations of the solar wind flow and magnetic field around the planets with no magnetic field: Calculation by a new MHD scheme. *J. Geophys. Res.* 98:17251–17262.

Wallis, M. K. 1972. Comet-like interaction of Venus with the solar wind I. *Cosmic Electrodyn.* 3:45–59.

Wu, C. C. 1992. MHD flow past an obstacle: Large scale flow in the magnetosheath. *Geophys. Res. Lett.* 19:87–90.

Zhang, M. H. G., et al. 1993. Oxygen ionization rates at Mars and Venus: Relative contributions of impact ionization and charge exchange. *J. Geophys. Res.* 98:3311–3318.

Zhang, T. L., Luhmann, J. G., and Russell, C. T. 1990. The solar cycle dependence of the location and shape of the Venus bow shock. *J. Geophys. Res.* 95:14961–14967.

Zhang, T. L., et al. 1993. On the spatial range of validity of the gas dynamic model in the magnetosheath of Venus. *Geophys. Res. Lett.* 20:751–754.